SAMPLE3D: A VERSATILE NUMERICAL TOOL FOR STUDYING GRAIN STRUCTURE AND TEXTURE OF MATERIALS PROCESSED BY POWDER BED FUSION ADDITIVE MANUFACTURING

Zerong Yang [a,*]**, Yves Kuesters** [b]**, Ruslan Logvinov** [b]**, Matthias Markl** [a] **and Carolin Körner** [a]

[a] Chair of Materials Science and Engineering for Metals (WTM)
Friedrich-Alexander-Universität Erlangen-Nürnberg (FAU)
Martensstr. 5, 91058 Erlangen, Germany

[b] Siemens AG, T AMM COA-DE
Siemensdamm 50, 13629 Berlin, Germany

* Correspondence: zerong.yang@fau.de

Key words: grain structure, texture, superalloy, powder bed fusion, additive manufacturing, numerical simulation, cellular automaton

Abstract. Powder Bed Fusion (PBF) not only enables the fabrication of metal parts with complex geometries in near-net-shape, but also offers the potential to tailor the microstructure and, consequently, the mechanical properties of the final product. In this contribution, we present our in-house developed simulation software $\mathbb{SAMPLE}^{3D}$ (Simulation of Additive Manufacturing on the Powder scale using a Laser or Electron beam in 3D), which is designed specifically for simulating grain structure evolution during PBF processes. The core of $\mathbb{SAMPLE}^{3D}$ is composed of a finite difference model and a cellular automaton model. The finite difference model is used to obtain the temperature field caused by an electron or laser beam. This temperature field is further used in the cellular automaton model to simulate grain structure development where grain selection as well as nucleation is considered. A range of information can be extracted from the simulation results, such as texture, grain morphology, and grain boundary arrangement. $\mathbb{SAMPLE}^{3D}$ provides a way to get insight into the relationship between PBF process strategies and microstructures. $\mathbb{SAMPLE}^{3D}$ has been employed to investigate the texture and grain structure evolution of various materials in different research projects.

1 INTRODUCTION

Powder Bed Fusion (PBF) is a class of additive manufacturing processes that utilize a high-energy beam to selectively fuse powder particles layer by layer, ultimately constructing customized parts from the powder bed [1]. PBF has emerged as a versatile technology capable of processing a wide range of materials, including metals, polymers, and ceramics. The energy beam commonly employed in PBF is either an electron beam (EB) or a laser beam (LB). In the context of metal PBF, in addition to the primary goal of fabricating defect-free parts, there is a rising interest in the manipulation of material microstructure such as grain morphology and crystallographic orientation. This can be achieved by varying process parameters and scanning strategies [2–4]. It is well-known that numerous properties of metallic materials heavily rely on their microstructural characteristics. However, traditional

experimental methods employed to study the effects of process conditions on microstructure are costly and time-consuming. Moreover, obtaining real-time insights into the details of microstructural evolution during PBF is challenging or even unfeasible through experimental approaches alone. In contrast, numerical simulation has emerged as an effective alternative method. Recent reviews [5, 6] have highlighted the growing role of numerical simulations in studying microstructure evolution during PBF. Numerical simulations can not only be used to aid in microstructure customization, but also enable an in-depth understanding of microstructural evolution during processing. While both PBF-LB and PBF-EB are similar technologies for metals, this work focuses on PBF-EB as an illustrative example to demonstrate the usefulness of SAMPLE³ᴰ.

Here, it is worth mentioning that the core of SAMPLE³ᴰ is based on a Cellular Automaton (CA) algorithm, which will be described in detail in Section 2. Similar CA-based algorithms have been utilized by different research groups to study the grain structure evolution during various additive manufacturing processes. For instance, Zinoviev et al. [7] employed a CA approach to simulate the grain structure evolution of 316L during PBF-LB. Although the simulation was performed in 2D, the simulation results exhibited similar characteristics to those observed in the experiments. Lawrence Livermore National Laboratory has developed the open-source software ExaCA for simulating alloy solidification [8], which is also based on a CA method. Additionally, Lian et al. [9] utilized a CA algorithm coupled with a finite volume method to investigate the grain structure evolution of INCONEL® 718 during the directed energy deposition (DED) process.

The microstructure predicted by SAMPLE³ᴰ has been experimentally validated for various materials and different PBF-EB process parameters [10–12]. Here, the microstructure mainly refers to the grain structure and texture. The effectiveness of SAMPLE³ᴰ in assisting microstructure customization was recently showcased in [3], where simulations were performed in parallel using different scanning strategies and the resulting microstructures were evaluated and compared. In our previous research, we employed an analytical solution [10] and numerical models [3, 11] to obtain the temperature field necessary for the microstructural simulation. In these thermal models, a 2D Gaussian beam is used as the heat source. However, additional efforts must be made to determine certain simulation parameters such as the absorptivity for the EB and the EB spot size, which are generally challenging to directly measure [13, 14].

Alternatively, the current contribution employs an equivalent heat source to circumvent these uncertainties, which offers higher efficiency and robustness in the thermal modeling. In Section 2, the core components of SAMPLE³ᴰ are introduced, encompassing a thermal model and a microstructural model. Emphasis is given to the equivalent heat source method. Section 3 shows a demonstration case for the up-to-date SAMPLE³ᴰ. Simulation results are compared with experimental findings. Significant emphasis is placed on the post-analysis of the 3D simulation data, highlighting the versatility and capabilities of the simulation software SAMPLE³ᴰ. Finally, we draw conclusions in Section 4.

2 NUMERICAL MODELS

2.1 Thermal model

Within the thermal model, the powder bed is approximated as an isotropic dense material. The heat equation with an external heat source and considering only heat conduction is given by [15]

$$c_\mathrm{p}\frac{\partial T}{\partial t} \equiv \frac{\partial H(T)}{\partial t} = \frac{\lambda}{\rho}\left(\frac{\partial^2 T}{\partial x^2} + \frac{\partial^2 T}{\partial y^2} + \frac{\partial^2 T}{\partial z^2}\right) + \frac{Q}{\rho}, \tag{1}$$

where c_p, λ and ρ are the specific heat capacity at constant pressure, thermal conductivity, and mass density of the material, respectively. Constant values of λ and ρ are used in the simulation, neglecting their temperature dependence. T is the temperature. t is the time. H is the enthalpy. Q is the external heat source term. x, y, z are the Cartesian coordinates. A conventional forward-time and central-space finite difference method [3] is employed to solve Equation (1). The enthalpy method [16] is used to handle the nonlinear behavior of specific heat during melting and solidification. The thermal boundary conditions are elucidated in Section 3.2 while detailing the simulation setup.

It is important to highlight the modeling of Q using the equivalent heat source approach. On the one hand, the utilization of equivalent heat sources offers the advantage of circumventing the challenges associated with determining certain simulation parameters, such as EB diameter and absorption depth. This alleviates the difficulty of obtaining precise measurements for these parameters, simplifying the modeling process. On the other hand, additional physical effects, such as heat convection and heat loss caused by evaporation, are implicitly accounted for during the construction of Q. Therefore, the utilization of the equivalent heat source approach facilitates a more realistic representation of the temperature field during the PBF process. The equivalent heat source [17] employed in this study is schematically shown in Figure 1, which has a conical frustum shape. The conical frustum shape is characterized by its top radius, bottom radius, and height, represented by r_t, r_b, and d, respectively. A line of energy $P_z(z)$ in units of W/m is distributed along the vertical axis from the top of the frustum to a depth of d. If a simulation cell is located within the frustum, it receives a power density of $P_z(z)/A(z)$ in units of W/m^3, where $A(z)$ represents the horizontal section area of the conical frustum at a specific depth, z. That is, for an arbitrary simulation cell with coordinates (x, y, z) at a certain time t, the power density it receives can be calculated by

$$Q(x,y,z,t) = \begin{cases} P_z(z)/(\pi r(z)^2) & z < d \text{ and } r(z) > \sqrt{(x_B(t)-x)^2 + (y_B(t)-y)^2}, \\ 0 & \text{otherwise,} \end{cases} \quad (2)$$

where $r(z)$ is the radius of the conical frustum at z, calculated by $r(z) = r_t - (r_t - r_b)z/d$. $x_B(t)$ and $y_B(t)$ give the position of the center axis of the beam in the x-y plane at a given time t. A detailed description of the method used to obtain the equivalent heat source is provided in Section 3.2.
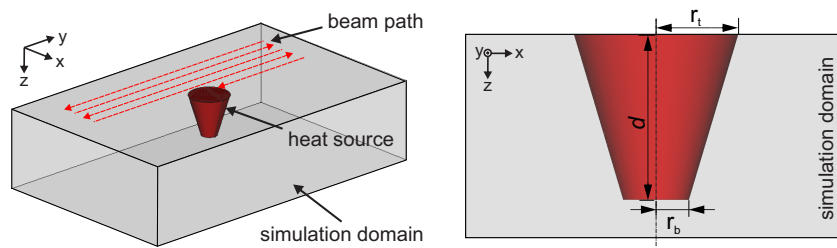

Figure 1: Schematic diagram of the equivalent heat source, which has a conical frustum shape and moves in the simulation domain following a predefined snake-hatch pattern (left). A 2D longitudinal section of the simulation domain (right).

2.2 Microstructural model

The microstructure, here mainly referring to the grain structure and texture, is modeled based on the 3D CA algorithm proposed by Gandin et al. [18]. This model is well documented in the series of

publications by Gandin et al. [18, 19] and Koepf el al. [10–12], and others [7, 8, 20]. Nevertheless, for the sake of completeness, it is briefly described as follows.

In the CA model, the focus is not on capturing precise dendrite shapes and other intricate associated details. Instead, individual dendrites are represented by superpositions of octahedra. Octahedra belonging to the same dendrite share the same crystallographic orientation, which is characterized by a set of Euler angles. Each octahedron is coupled to a distinct simulation cell, and its major axes coincide with the $\langle 100 \rangle$ growth directions. Therefore, the presented CA model is restricted to applications to materials where the preferential growth direction of dendrites is $\langle 100 \rangle$. So far, the CA model has predominantly been applied to study nickel-based superalloys, such as INCONEL[®] 718 [10], CMSX-4[®] [3, 11] and in the current work ABD[®]-900AM. These alloys possess face-centered cubic (FCC) crystal structures and exhibit a preferential growth direction along the $\langle 100 \rangle$ crystallographic orientation. The growth velocity of an octahedron v_{oct} is determined by the local undercooling ΔT of its associated cell. In principle, different types of undercooling, such as curvature undercooling and thermal undercooling, contribute to the overall undercooling ΔT. However, the current work only considers the most important undercooling during solidification in the PBF-EB process, namely, thermal undercooling. Once the facet of the growing octahedron reaches the center of a neighboring cell, that cell is integrated into the dendrite and at the same time a new octahedron is initiated at that cell.

A nucleation model has been recently developed and coupled to the 3D CA model [12]. As demonstrated in the next section, nucleation has been found to play an insignificant role under the current processing conditions in both the experimental and simulation results. The simulation results obtained without employing the nucleation model already exhibit a satisfactory agreement with the corresponding experimental results. Nevertheless, future investigations should be conducted to determine the appropriate nucleation parameters for various materials, thus strengthening the predictive power of the CA model [5].

3 APPLICATION EXAMPLE

This section begins by describing the experimental setup in Section 3.1 and the simulation setup in Section 3.2. The subsequent section, Section 3.3, focuses on the comparison between the simulation and experimental results. Finally, in Section 3.4, post-analysis is performed based on the simulation results, showcasing the versatility of S𝔸𝕄ℙLE[3D].

3.1 Experimental procedure

Sample creation. Cuboid samples of $15(W) \times 15(L) \times 12(H)\,\text{mm}^3$ were fabricated using a modified Arcam A2 PBF-EB machine (Arcam AB, Sweden and Pro-beam systems GmbH, Germany). The feedstock material for the PBF-EB process was ABD[®]-900AM metal powder (OxMet Technologies Ltd., UK) with a particle size ranging from $45\,\mu\text{m}$ to $106\,\mu\text{m}$. The chemical composition of the main alloying elements (> 1 wt.%) is shown in Table 1, which was provided by the manufacturer.

Table 1: Chemical composition of as-received ABD[®]-900AM powder.

	Ni	Cr	Co	Mo	W	Al	Ti	Ta	Nb
wt.%	Bal.	17.0	20.1	2.1	3.1	2.2	2.3	1.5	1.8

The first 2 mm height of the sample served as a full-support structure, created using a beam power of 800 W. Whereas the upper part was built using a higher beam power of 950 W. The beam speed

and diameter were consistent for both the support and the structure above it, set as $5\,\text{m/s}$ and $470\,\mu\text{m}$, respectively. The beam diameter was an approximate value determined according to the $1/e^2$ method. Throughout the build process, the powder layer thickness was maintained as $50\,\mu\text{m}$. The measured temperature at the baseplate was approximately $1070\,^\circ\text{C}$. A cross-snake hatch scanning strategy was employed, with a line offset of $100\,\mu\text{m}$. After each layer, the scan pattern was rotated by 90°.

Characterization. The samples were sectioned both longitudinally and transversely for analysis. Both the longitudinal and transverse sections were taken approximately from the middle of the specimen. These cross-sections underwent metallographic preparation and etched with Kalling's No. 2 etchant. Microscopic analysis was conducted on these cross-sections using a light microscope and a scanning electron microscope. Furthermore, electron backscatter diffraction (EBSD) measurements were performed on the cross-sections to determine the crystallographic orientations of the grains.

3.2   Simulation setup

The simulation setups for $\mathbb{SAMPLE}^{3D}$ can be categorized into three main aspects: simulation domain, material parameters, and reconstructed equivalent heat source.

Simulation domain. The simulation domain has a size of $27(W) \times 27(L) \times 1(H)$ mm³, with a simulation cell size of $\Delta x = 25\,\mu\text{m}$. The time step used for the thermal simulation is $\Delta t = 2.5\,\mu\text{s}$, which satisfies the von Neumann stability criterion [21] and ensures sufficient steps for the EB energy deposition in each simulation cell. During the simulation, the heat source moves according to the predefined scan pattern, mimicking the EB snake hatching strategy employed in the PBF-EB experiment. Since the simulation domain is significantly larger in the horizontal dimension than the experimental sample and much larger in the longitudinal dimension than the melt pool depth that will be described later, the heat flux across the surface of the simulation domain is neglected. This means that the simulation domain is treated as an isolated system, with the only energy input coming from the heat source.

For the CA simulation, $\Delta t = 10\,\mu\text{s}$ is used to ensure that the octahedron does not grow more than $1/10$ of Δx within one time step. One might notice that the simulation domain in the z direction is significantly smaller than the actual height of the part to be built. This is a deliberate choice made to optimize computational efficiency and is referred to as the simulation domain truncation mechanism. After completing one layer, the CA simulation results at the bottom of the domain with one layer thickness are exported. The remaining portion of the domain is then shifted downward by two cell sizes, and the top of the domain is repopulated with cells possessing random crystallographic orientations. This process mimics the lowering of the powder bed and deposition of a new powder layer in the experiment. Finally, the simulation results are merged to obtain the full height of the part. In addition to the simulation domain truncation mechanism, the thermal field reuse mechanism [11] and Message Passing Interface (MPI) parallelization [12] are used to further speed up the simulation.

Material parameters. The material parameters are obtained or derived from the ABD®-900AM data sheet [22]. $\rho = 8395\,\text{kg/m}^3$ and $\lambda = 27\,\text{W/(m K)}$ are used as constants by neglecting their temperature dependence. However, the temperature-dependent H is required for the enthalpy method. H evolves with the simulation time step, and the corresponding temperature T is obtained from the $H - T$ relationship. $H(T)$ is derived from the temperature-dependent specific heat capacity data. The $H - T$ curve is depicted in Figure 2a, taking H at the room temperature as a reference.

Phase transition temperatures and the undercooling-dependent octahedron growth velocity $v_{\text{oct}}(\Delta T)$ are needed for the CA simulation. The solidus temperature $T_s = 1287\,^\circ\text{C}$ and liquidus temperature $T_l = 1362\,^\circ\text{C}$ are obtained from the material data sheet [22]. Since the chemical composition of
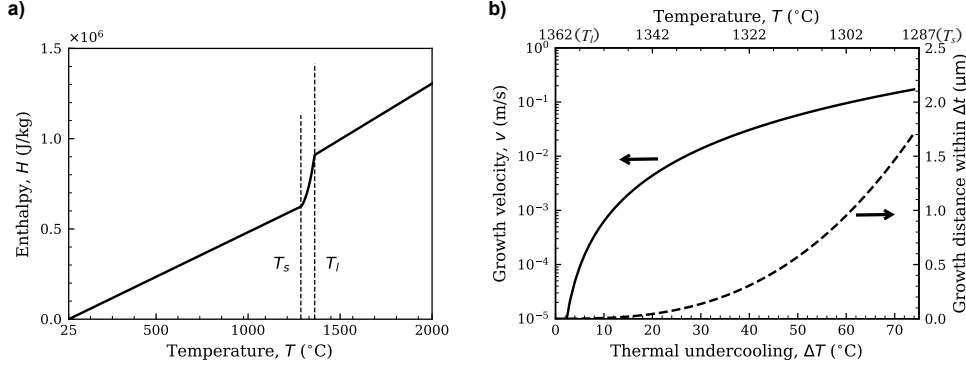
Figure 2: (a) Enthalpy as a function of temperature, taking the value at the room temperature as a reference. H is linearly extrapolated in the region of $T > 2000\,°C$. The solidus temperature $T_s = 1287\,°C$ and liquidus temperature $T_l = 1362\,°C$ are marked for reference. (b) Octahedron growth velocity (left axis) and growth distance within one time step ($\Delta t = 10\,\mu s$) (right axis) as a function of thermal undercooling. The temperature range from T_l to T_s is added to the top axis for reference.

ABD®-900AM is similar to that of INCONEL® 718, $v_{oct}(\Delta T)$ developed for INCONEL® 718 is adopted in this work, which is given by [12]

$$v_{oct}(\Delta T) = 1 \cdot 10^{-6} (\Delta T)^{2.8} \quad \text{with } \Delta T = T - T_l. \tag{3}$$

It is worth noting that Equation (3) was obtained by fitting to phase field simulation data [12]. $v_{oct}(\Delta T)$ is plotted in Figure 2b. The growth distance of an octahedron within one time step ($\Delta t = 10\,\mu s$) is also shown as a function of ΔT for reference.

   Reconstructed equivalent heat source. It characterizes the power distribution within its volume, ensuring that the thermal simulation accurately reproduces the experimentally observed melt pool geometry. To reconstruct the heat source, the experimentally obtained melt pool profile from a longitudinal cross-section was utilized, with the melt pool width measured at various depths, denoted as $w_{exp}(z)$. The heat source reconstruction aims to achieve a simulated temperature field that produces the same melt pool profile, $w_{sim}(z)$, as $w_{exp}(z)$. This inverse problem was solved using the algorithm described in [23], considering PBF process parameters such as beam speed. To incorporate the effect of heat convection in the melt pool, the values of λ were multiplied by a factor of 3 when $T \geq T_l$.

   The parameters in the heat source model, specifically $P_z(z)$ and $r(z)$ (see Equation (2)), were determined through an iterative process. The goal was to minimize the discrepancy between $w_{sim}(z)$ and $w_{exp}(z)$. This involved recursively computing $w_{sim}(z)$ while adjusting $P_z(z)$ and $r(z)$ until a satisfactory agreement was achieved. The initial distribution of $P_z(z)$ was set to be proportional to $w_{exp}(z)$, and the initial $r(z)$ was assumed to be 90% of $w_{exp}(z)$ at the same z coordinate. The resulting frustoconical heat source exhibits geometric parameters of $r_t = 450\,\mu m$, $r_b = 400\,\mu m$, and $d = 70\,\mu m$. Figure 3a shows the distribution of the heat source $P(z)$, where linear interpolation was applied to estimate values between the scatter data points. It is noteworthy that $P(z) = 0$ when $z > 50\,\mu m$, indicating that the maximum deposition depth of the heat source is 50 µm, even though $d = 70\,\mu m$. Figure 3b shows a comparison between the melt pool profile predicted by $\mathbb{SAMPLE}^{3D}$ and the experimentally obtained melt pool geometry. The experimental measurements yield a melt pool depth of 78.7 µm and a half width of 399.2 µm. In contrast, the $\mathbb{SAMPLE}^{3D}$ simulation predicts a melt pool depth of 75.0 µm and a half width of 362.5 µm. The close agreement between the predicted and measured values validates the accuracy of the equivalent heat source approach employed in $\mathbb{SAMPLE}^{3D}$.

The discrepancy observed in the flanks of the melt pool is considered to be not important, since they are remelted during the processing of neighboring lines in a snake-hatch scanning pattern, except for the very edge ones. This slight discrepancy might be attributed to the omission of the temperature dependence of some material properties, such as ρ and λ, in the thermal simulation. Nevertheless, this validation provides confidence in the reliability of using the equivalent heat source approach for simulating the PBF-EB process across multiple layers.
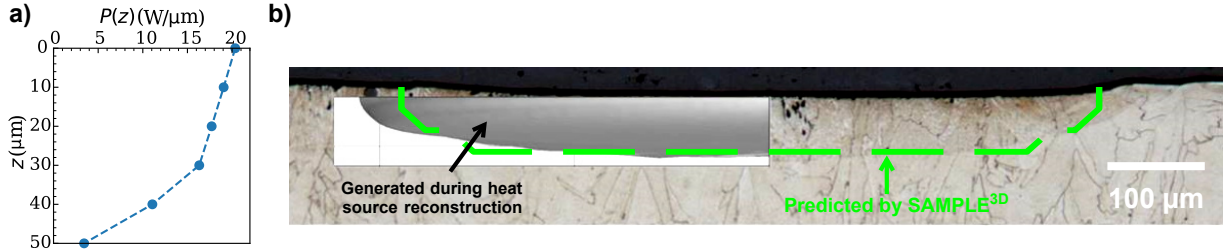
Figure 3: (a) The distribution of the linear energy source $P(z)$ along the depth. The scatter data points serve as input for $\mathbb{SAMPLE}^{3D}$, and values between the data points are linearly interpolated. (b) A comparison between the simulation-predicted melt pool profile and the experimentally obtained melt pool geometry.

3.3   Comparison of simulation and experimental results

Figure 4 presents the comparison between the simulation and experimental results in the longitudinal cross-section. For convenience, from now on, the direction of the z-axis is shifted upward parallel to the build direction (BD), instead of downward as shown in Figure 1. Figure 4a shows that the simulated microstructure exhibits similar features and characteristics to the experimental micrograph. Both exhibit distinct regions, namely the shell region and the core region. In the shell region, the grains grow obliquely from the outer edge inward, while in the core region, the grains grow vertically from the bottom to the top. The width of the shell region predicted by the simulation matches well with the measurement from the optical micrograph, both approximately 2 mm. In terms of crystallographic orientation, the simulated micrograph shows a nearly random distribution of grain orientations in the shell region, whereas the core region exhibits a strong {100} texture. Further comparison with experimental EBSD results will be presented below to validate these findings.

In order to further compare the simulation and experimental results, the average grain widths were measured using the intercept method at different build heights for both the core and shell regions. The measurement positions are indicated by the horizontal black and white lines in Figure 4a, and the measurement results are shown in Figure 4a-b, for the core and shell regions, respectively. In general, the comparison between the simulation and experimental data shows good agreement, with a slight discrepancy observed at the lower position for the grain size in the shell region. In both the simulation and experiment, the grains in the core region undergo significant horizontal expansion with increasing build height. The grains initially start as small with a width of around 25 μm, then undergo a transition zone with a height of approximately 5 mm, and finally, in the upper region, they exhibit an average grain width of approximately 300 μm. The small discrepancy mentioned above is considered to be attributed to the different beam powers used in the simulation (950 W) and the experiment (800 W).

Figure 5 depicts the comparison between the simulation and experimental results in the transversal cross-section in the core region. In Figure 5a, the predicted microstructure is compared to the experimentally obtained EBSD inverse pole figure (IPF) maps. The comparison reveals that both the
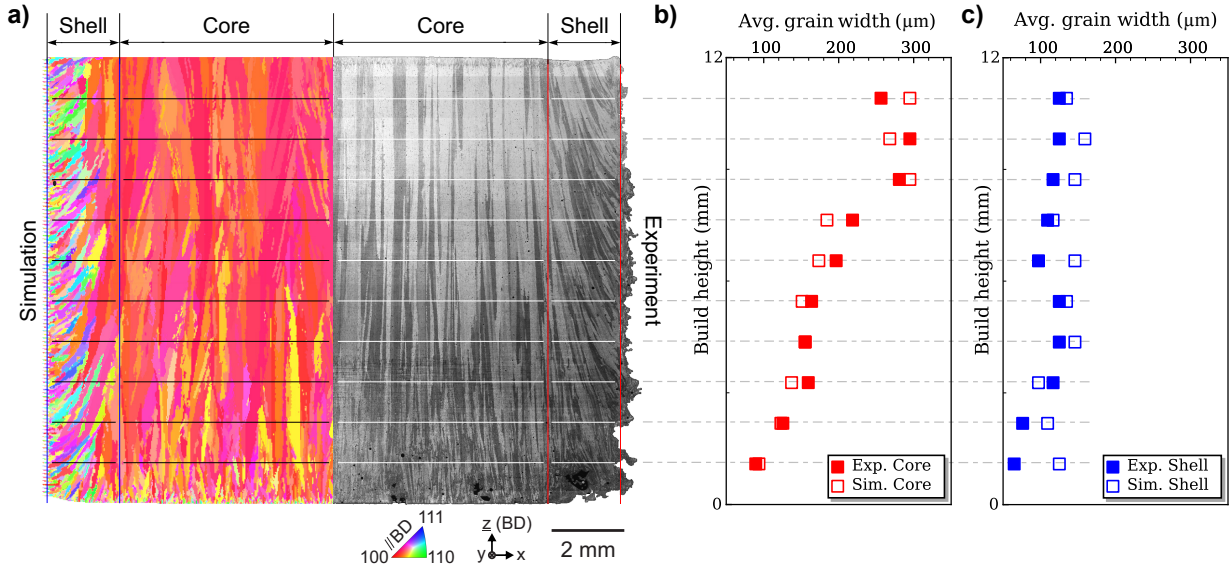
Figure 4: (a) Comparison between the SΛMPLE³ᴰ-predicted microstructure and the experimentally obtained optical micrograph in the longitudinal cross-section. (b-c) Comparison of SΛMPLE³ᴰ-predicted and experimentally measured average grain widths at different build heights in the core region and the shell region, respectively. The measurement positions for the average grain widths are indicated by horizontal black and white lines in (a).

experiment and simulation exhibit a dominance of {100} crystallographic orientation in the core region, with the z axis or BD as reference. To quantitatively describe the crystallographic orientation distribution, orientation distribution function (ODF) pole figures were generated using the MTEX toolbox [24], as shown in Figure 5b. Once again, the ODF pole figures obtained from the simulation data and experimental data exhibit a strong agreement, showcasing a significant {100} texture.
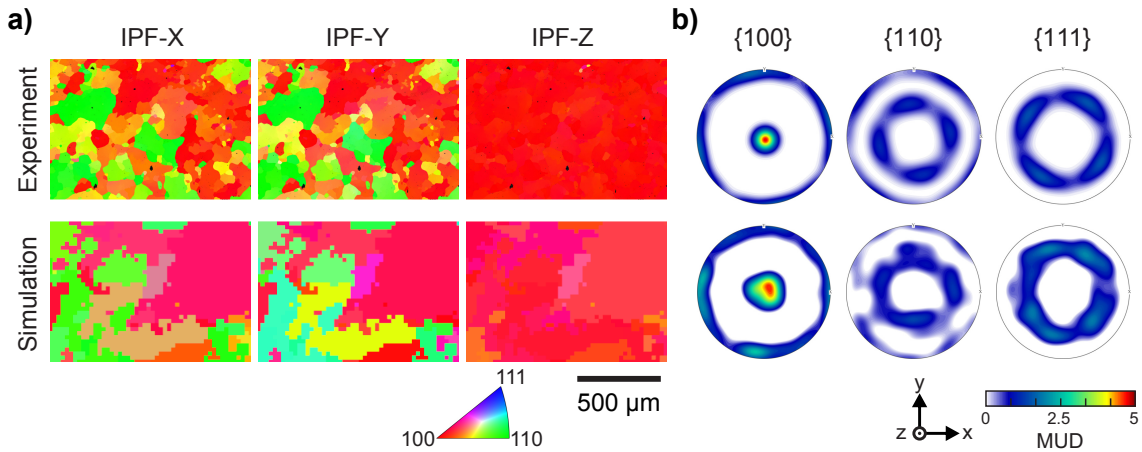

Figure 5: (a) Comparison between the SΛMPLE³ᴰ-predicted microstructure and the experimentally obtained EBSD inverse pole figure (IPF) maps in the transversal cross-section. (b) Comparison of orientation distribution function (ODF) pole figures generated from the data shown in (a).

So far, the comparison between the simulation and experimental data in both the longitudinal and transversal cross-sections reveals excellent agreement. This demonstrates the capability of SΛMPLE³ᴰ

to accurately capture the grain structure development during the PBF-EB process. The close agreement between the simulation and experimental results allows us to further explore and extract valuable information from the simulation data, as detailed in the following. It is important to emphasize that the data presented below is difficult or even impossible to access using experimental methods.

3.4   Mining the simulation results

In this section, the simulation data is further analyzed to leverage the benefits of 3D simulation. Due to the symmetry of the sample and the scanning strategy employed, the analysis presented below focuses on 1/4 of the cuboid. Specifically, the complete simulation domain is divided in the middle along the x and y dimensions, and one of the 1/4-domains is used for analysis.

3D texture analysis. The ODF pore figures presented in the previous section were derived from 2D sections of the simulation domain and 2D experimental EBSD data. These approaches can provide only limited information compared to a comprehensive 3D analysis. However, performing EBSD analysis in 3D can be very time-consuming and expensive. In contrast, the 3D simulation data can be evaluated relatively easily still using MTEX. This allows for a comprehensive assessment of the texture in 3D without the need for extensive experimental measurements.

In Figure 6, it can be observed that the strongest intensity is associated with the {100} orientations for both the entire and core regions of the 1/4-domain. Additionally, in the shell region, the intensity in {100} is slightly stronger than those in {110} and {111}, but it is much less pronounced compared to the entire and core ones. This indicates that the strong {100} texture observed in the entire sample is primarily influenced by the strong {100} texture present in the core region.
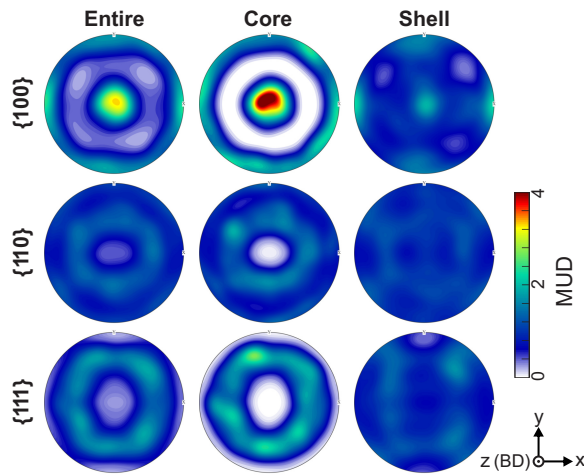

Figure 6: Orientation distribution function (ODF) pole figures constructed using the entire (left), core (middle), and shell (right) regions of the 1/4 3D crystal orientation data. Intensity is displayed in units of multiple of uniform distribution (MUD).

Grain size distribution. The grain size was analyzed by examining the grain area distributions at different heights within the 1/4-domain. The results are shown in Figure 7, revealing distinct behaviors of the grains in different regions. The grains in the shell region consistently exhibit small sizes without significant expansion horizontally as the build height increases. On the other hand, the grains in the core region demonstrate substantial horizontal expansion with increasing build height. Figure 7 highlights the contrasting growth patterns of grains in different regions of the printed sample.

Grain aspect ratio. For this evaluation, each grain is treated as a cylinder with the same volume and length as the grain, and the grain aspect ratio is determined by calculating the ratio of the estimated grain length to the estimated grain diameter, as illustrated in Figure 8a. The resulting aspect ratio
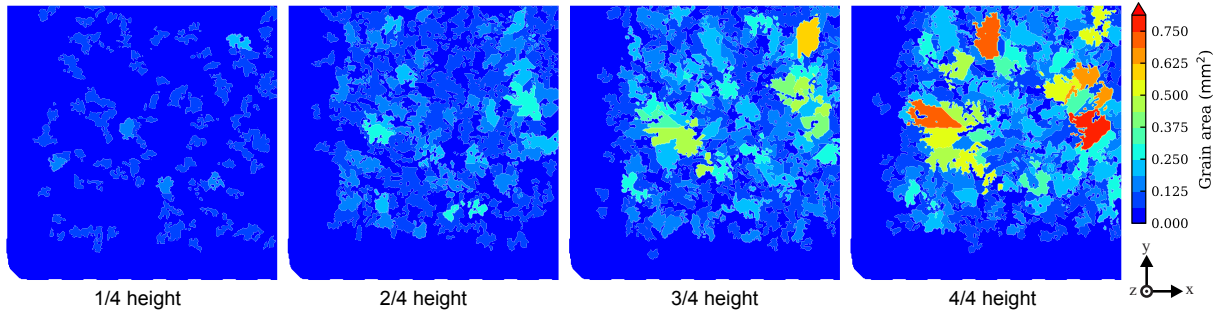
Figure 7: Grain size distribution at different heights within the 1/4-domain.

values are presented in Figure 8b. In general, the grains in the core region exhibit the highest aspect ratio, indicating the presence of more elongated, fiber-like grains in this region.
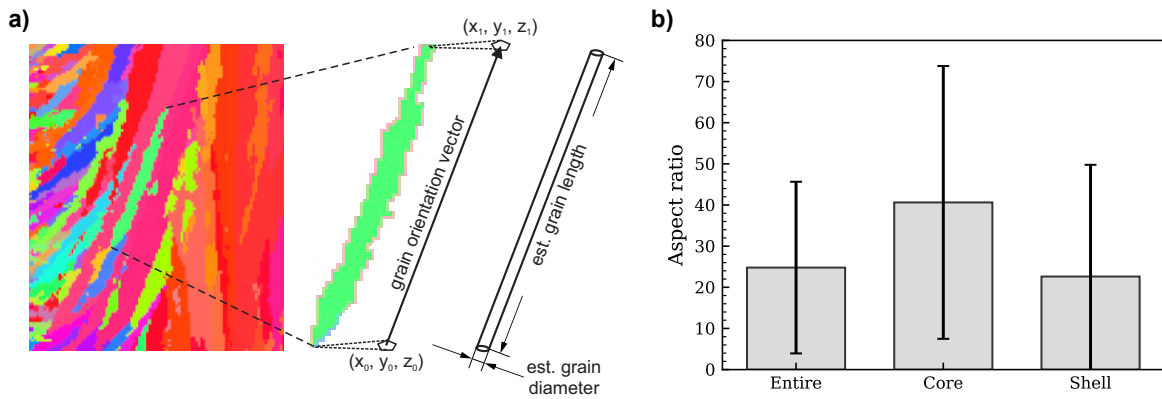

Figure 8: (a) Schematic showing the definition of the grain orientation vector and the estimation of grain length and diameter. (b) Grain aspect ratios evaluated in different regions.

Grain boundary arrangement. Figure 4a has shown that a significant portion of grains in the core region exhibit vertical growth from the bottom to the top, while the grains in the shell region display a growth pattern from the outside towards the core region with an inclination. To assess the arrangement of grain boundaries in 3D, the grain orientation vectors were computed within the 1/4-domain. The grain orientation vector is defined as a vector that originates from the center of the lowest section of the grain and extends to the center of the highest section of the grain, as illustrated in Figure 8a. The grain orientation vectors were statistically evaluated using the MTEX toolbox, with each vector being weighted by the corresponding grain volume.

Figure 9 depicts the pole figures of the grain orientation distribution, shedding light on the arrangement of grain boundaries. The pole figures reveal that the grain orientation vectors in the core region are predominantly aligned parallel to the z axis. Conversely, the non-parallel-to-z axis grains are primarily concentrated in the shell region. It is worth noting that the grain orientation distribution for the complete simulation domain can be estimated by utilizing the symmetry of the sample and the results from the 1/4-domain.

4   CONCLUSIONS

In this study, we present the up-to-date $\mathbb{SAMPLE}^{3D}$ simulation software, a comprehensive and powerful tool designed specifically for simulating the evolution of grain structures in 3D during PBF
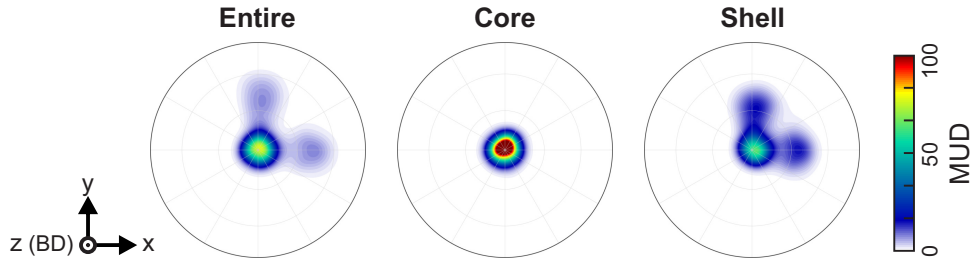
Figure 9: Pole figures of grain orientation distribution constructed based on the grain orientation vectors obtained from the entire (left), core (middle), and shell (right) regions of the 1/4 3D simulation domain. Intensity is displayed in units of multiple of uniform distribution (MUD).

processes. The utilization of equivalent heat source is highlighted, which overcomes the challenge of determining difficult-to-measure simulation parameters. By comparing the simulation results with PBF-EB experimental findings, we demonstrate the robustness and accuracy of SAMPLE³ᴰ.

Furthermore, we showcase the versatility of SAMPLE³ᴰ through post-analysis of the 3D simulation data. This post-analysis provides valuable insights into various aspects of the grain structure, including texture, grain size distribution, grain aspect ratio, and grain boundary arrangement. These insights are difficult to obtain experimentally, highlighting the advantage of using SAMPLE³ᴰ for studying the grain structure evolution in PBF processes.

Additionally, we would like to mention our previous work where we have demonstrated the utility of SAMPLE³ᴰ simulation results for generating representative volume elements (RVEs) and assisting in up-scaling micromechanical simulations and homogenization, as presented in [4]. This further underscores the usefulness of SAMPLE³ᴰ in the field of additive manufacturing research.

References

[1] I. Gibson, D. Rosen, B. Stucker, M. Khorasani, Powder Bed Fusion, in: Additive Manufacturing Technologies, Springer International Publishing, 2020, pp. 125–170.

[2] H. Helmer, A. Bauereiß, R. Singer, C. Körner, Grain structure evolution in Inconel 718 during selective electron beam melting, Materials Science and Engineering: A 668 (2016) 180–187.

[3] Z. Yang, J. A. Koepf, M. Markl, C. Körner, Numerical prediction of texture and grain structure in additively manufactured lattice struts, Progress in Additive Manufacturing (submitted) (2023).

[4] Z. Yang, L. Herrnböck, M. Markl, J. Mergheim, P. Steinmann, C. Körner, Mesoscopic modeling and simulation of properties of additively manufactured metallic parts, in: Collaborative Research Center 814: Additive Manufacturing, Springer (in press), 2023.

[5] C. Körner, M. Markl, J. A. Koepf, Modeling and simulation of microstructure evolution for additive manufacturing of metals: a critical review, Metallurgical and Materials Transactions A 51 (2020) 4970–4983.

[6] D. R. Gunasegaram, I. Steinbach, Modelling of microstructure formation in metal additive

manufacturing: Recent progress, research gaps and perspectives, Metals 11 (2021) 1425.

[7] A. Zinoviev, O. Zinovieva, V. Ploshikhin, V. Romanova, R. Balokhonov, Evolution of grain structure during laser additive manufacturing. simulation by a cellular automata method, Materials & Design 106 (2016) 321–329.

[8] M. Rolchigo, S. T. Reeve, B. Stump, G. L. Knapp, J. Coleman, A. Plotkowski, J. Belak, Exaca: A performance portable exascale cellular automata application for alloy solidification modeling, Computational Materials Science 214 (2022) 111692.

[9] Y. Lian, Z. Gan, C. Yu, D. Kats, W. K. Liu, G. J. Wagner, A cellular automaton finite volume method for microstructure evolution during additive manufacturing, Materials & Design 169 (2019) 107672.

[10] J. A. Koepf, M. R. Gotterbarm, M. Markl, C. Körner, 3D multi-layer grain structure simulation of powder bed fusion additive manufacturing, Acta Materialia 152 (2018) 119–126.

[11] J. A. Koepf, D. Soldner, M. Ramsperger, J. Mergheim, M. Markl, C. Körner, Numerical microstructure prediction by a coupled finite element cellular automaton model for selective electron beam melting, Computational Materials Science 162 (2019) 148–155.

[12] J. A. Koepf, M. R. Gotterbarm, C. Kumara, M. Markl, C. Körner, Alternative approach to modeling of nucleation and re-melting in powder bed fusion additive manufacturing, Advanced Engineering Materials (2023).

[13] A. Klassen, Simulation of evaporation phenomena in selective electron beam melting, FAU University Press, 2018.

[14] M. Reith, C. Breuning, M. Franke, C. Körner, Impact of the power-dependent beam diameter during electron beam additive manufacturing: a case study with γ-TiAl, Applied Sciences 12 (2022) 11300.

[15] H. S. Carslaw, Conduction of heat in solids, Clarendon Press, 1986.

[16] L. W. Hunter, J. R. Kuttler, The enthalpy method for heat conduction problems with moving boundaries, Journal of Heat Transfer 111 (1989) 239–242.

[17] F. Farrokhi, B. Endelt, M. Kristiansen, A numerical model for full and partial penetration hybrid laser welding of thick-section steels, Optics and Laser Technology 111 (2019) 671–686.

[18] C.-A. Gandin, M. Rappaz, A 3D cellular automaton algorithm for the prediction of dendritic grain growth, Acta Materialia 45 (1997) 2187–2195.

[19] C.-A. Gandin, M. Rappaz, A coupled finite element-cellular automaton model for the prediction of dendritic grain structures in solidification processes, Acta Metallurgica et Materialia 42 (1994) 2233–2246.

[20] Y. Lian, S. Lin, W. Yan, W. K. Liu, G. J. Wagner, A parallelized three-dimensional cellular automaton model for grain growth during additive manufacturing, Computational Mechanics 61 (2018) 543–558.

[21] K. A. Hoffmann, S. T. Chiang, Computational fluid dynamics (vol. 1), Engineering Education System, 2000.

[22] Aubert & Duval, ABD®-900AM data sheet, 2023. URL: https://www.aubertduval.com/wp-media/uploads/sites/2/2019/09/ABD-900AM_PearlMicro_AM_V2ter__GB.pdf.

[23] V. Yerofeyev, R. Logvinov, V. Nesterenkov, A. Mazo, Formation of the equivalent heat source for calculating strains in structures in electron beam welding, Welding International 28 (2013) 557–561.

[24] F. Bachmann, R. Hielscher, H. Schaeben, Texture analysis with MTEX - free and open source software toolbox, Solid State Phenomena 160 (2010) 63–68.